ORIGINAL PAPER

Towards FIB-SEM Based Simulation of Pore-Scale Diffusion in SCR Catalyst Layers

J. Proff[1,2] · M. Mail[3] · A. Lindner[4] · A. Scheuer[2] · M. Bendrich[2] · E. Quinet[2] · A. Schuler[2] · T. Scherer[3] · C. Kübel[1,3] · M. Votsmeier[1,2]

Abstract
The diffusivity in the upper Cu-Chabazite layer of a dual layer ammonia oxidation catalyst with a lower Pt layer was investigated. In a first step, the pore structure of the upper Cu-Chabazite catalyst layer was determined by Focused Ion Beam-Scanning Electron Microscopy (FIB-SEM) slice&view tomography. From the FIB-SEM data the 3D pore structure of the catalyst was reconstructed and diffusion simulations were performed on the reconstructed pore geometry, resulting in an estimated effective diffusivity of $D_{eff}/D_{gas} = 0.31$. To validate the FIB-SEM derived estimates of the diffusivity, measurements of CO oxidation on the dual layer catalyst were performed, where the CO was oxidized in the lower Pt-layer while the upper SCR layer served as an inactive diffusion barrier. In this way, the effective diffusivity can be determined from the measured CO conversion. An effective diffusion coefficient of $D_{eff}/D_{gas} = 0.11$ was obtained from the CO oxidation measurements, three times lower than the value obtained from the FIB-SEM data, but in line with previous literature data for the effective diffusivity in monolith washcoat layers. Additional NH_3 oxidation experiments were performed on the dual layer catalyst. The results were well reproduced by a reactor model applying the effective diffusion coefficient obtained by the CO oxidation experiments. The origin of this apparent inconsistency is currently not understood and requires further investigation.

1 Introduction

To achieve the required contact area, catalysts generally exhibit a micro-scale pore structure. Besides the intrinsic activity of the catalytic sites, catalyst performance is controlled by diffusion inside this pore structure. To date, simulation approaches do not explicitly consider the micro-scale effects, but rather use volume averaged effective diffusion coefficients and reaction rates obtained from macroscopic measurements of catalytic activity. Frequently, these volume averaged effective diffusivities D_{eff} are related to the bulk gas diffusivity D_{gas} and the porosity ε of the pore structure using a so-called tortuosity factor τ:

$$D_{eff} = \frac{\varepsilon}{\tau} D_{gas} \tag{1}$$

In this equation, the tortuosity factor τ is used as a fitting parameter that describes the effect of the pore geometry on the effective diffusion. It can be loosely interpreted as a parameter describing the effect of the increased effective path length through the tortuous pore structure.

Alternatively, when catalysts with different porosity are to be compared, it is convenient to report relative effective diffusivities D_{eff}/D_{gas}.

Such a macroscopic treatment of the pore scale diffusion in many cases yields an accurate description of the catalyst performance, and the resulting models are successfully applied towards the optimization of the macroscopic catalysts design. However, a rational optimization of the microstructure requires characterization techniques and simulation models that explicitly resolve the pore-scale. Furthermore,

✉ M. Votsmeier
  martin.votsmeier@tu-darmstadt.de

1 Technical University Darmstadt, 64287 Darmstadt, Germany

2 Umicore AG & Co. KG, 63457 Hanau-Wolfgang, Germany

3 Karlsruhe Nano Micro Facility (KNMF) and Institute of Nanotechnology (INT), Karlsruhe Institute of Technology (KIT), 76344 Eggenstein-Leopoldshafen, Germany

4 Institute for Applied Materials (IAM-ET), Karlsruhe Institute of Technology (KIT), 76135 Karlsruhe, Germany

todays modelling approach determines the effective diffusion coefficients together with the kinetic parameters from the same set of experiments, resulting in some correlation in the determined parameters. Determining the effective diffusivity from micro-scale geometry data will add independent information and will thus increase the quality of the kinetic parameters and the overall models. It has also been suggested that changes in the micro pore structure resulting in a dramatic decrease in effective diffusivity are a major mechanism of thermal ageing in exhaust catalysts [1]. The verification and quantification of such ageing models will require an independent experimental characterization of the pore structure and a detailed understanding how structural changes at the micro-scale can influence macroscopic catalyst performance.

Today experimental methods have become available that allow characterization of the catalysts 3D pore structure with nanometer resolution. These include X-ray nano tomography (CT), focused ion beam combined with scanning electron microscopy (FIB-SEM) and ptychographic X-ray microscopy. Fam et al. apply FIB-SEM and ptychographic X-ray tomography on ceria-doped nanoporous gold (CeO_x/np-Au) with 15–45 nm and 23 nm resolution respectively [2]. Becher et al. used ptychographic x-ray computed nanotomography for mapping the pore architecture of a Pt/Al_2O_3 diesel oxidation catalyst [3].

FIB-SEM has been used to perform nanoscale tomography on porous media for 3D reconstruction of the pore geometry [4–7]. Reising et al. used 3D reconstruction by FIB-SEM for simulations of the flow in high pressure liquid chromatography columns [8].

Pore geometries obtained by X-ray tomography have been used to simulate the reactive flow in the porous wall of catalytically coated filters [9–11]. Coated filters have relatively large pores > 10 μm so that resolution requirements are not as high as for coated monolith or pellet catalysts that generally exhibit pore sizes around 1 μm. So far, pore scale simulations of the catalyst in coated monoliths and pellets have been mostly performed on digitally reconstructed geometries based on SEM [12–14]. Karakaya et al. applied FIB-SEM based geometries to simulate the reaction–diffusion in representative individual pores [15].

It is well established that under typical operating conditions zeolite-based SCR catalysts can experience diffusion limitations. Nova et al. studied the SCR reaction in a Cu-zeolite by varying the cell density of the substrate at constant catalyst loading, therefore affecting only the thickness of the washcoat layer [16]. Reduced conversion was observed for the samples with increased washcoat thickness, demonstrating the relevance of pore-scale diffusion limitations. Along similar lines, Metkar et al. demonstrated the presence of diffusion limitations in Fe-ZSM-5

catalysts by varying the monolith length at constant overall catalyst loading per sample [17]. Yu et al. demonstrated the importance of diffusion limitations in a Cu-ZSM5 catalyst in a modelling study [18].

Diffusion limitation is especially important in dual layer systems where the reactants must diffuse through the upper layer to react on the lower layer. One example for such dual-layer systems is the ammonia slip catalyst (ASC) with a supported Pt catalyst in the bottom layer and an SCR catalyst in the upper layer. This concept allows for NO formed in the unselective Pt-containing lower layer to react with NH_3 in the upper SCR layer, reducing NO output and increasing N_2 selectivity. The performance of the dual layer ASC is critically influenced by diffusion in the upper SCR layer [14, 19–21], and fitting simulation models of the dual layer catalyst to experimental NH_3 conversion allows determining the effective diffusivity in the SCR layer [20]. Dhillon et al. showed that enhancing the macro-porosity of the zeolite layer yields a considerable improvement in the NH_3 conversion of the dual layer catalyst [22].

Using a probe reaction that is only active in the lower layer has been demonstrated as an approach to experimentally determine the effective diffusion coefficient of the upper layer, that in this case acts as pure diffusion resistance [13, 23]. Novák et al. applied this approach to determine the effective diffusion coefficients of alumina washcoats via CO oxidation. Shresta et al. studied NH_3 oxidation on a dual layer system with a blind Na-exchanged ZSM-5 zeolite layer on top of a Pt/Al_2O_3 layer.

In this work, we determine the 3D pore structure of an SCR layer in an ASC model catalyst using FIB-SEM tomography. The pore structure is reconstructed and diffusion simulations are performed on the obtained 3D structure to determine effective diffusion coefficients for the upper layer. Additionally, to validate the FIB-SEM based effective diffusion coefficients, the effective diffusivity of the top layer is experimentally determined by measuring the CO oxidation on the dual layer catalyst. In these measurements, the upper layer acts as an inactive diffusion barrier, which allows straightforward computation of the effective diffusivity from the observed conversion. Finally, simulations of ammonia oxidation on the dual layer catalyst are performed taking into account the reactions in both the upper SCR- as well as the lower Pt layer. The simulations are performed using the effective diffusion coefficients obtained from the FIB-SEM analysis and from the CO oxidation experiments. The respective simulation results are compared to the experimentally measured NH_3 conversion over the dual layer catalyst, hence providing a validation of the effective diffusion coefficients obtained by FIB-SEM and by the CO oxidation experiments.

2 Methods

For all experiments and measurements, cores of a dual layer model catalyst have been used, which were drilled from the full part. The model catalyst is a cordierite substrate with hexagonal channels coated with a Pt bottom layer (AOC) and a Cu-Chabazite top layer (SCR). The hexagonal channels cause the washcoat layer to be approximately circular (see Fig. 1).

2.1 FIB-SEM characterization

2.1.1 Sample preparation for FIB-SEM

In a first preparation step, slices with a thickness of about 5 mm were cut from the drill cores using a cut-off machine (ATM) with a diamond blade and water as a cooling agent. The speed of the saw was 2000 rpm and the automatic feed was 0.05 mm/s.

Using a tweezer, small pieces have been broken off the slices in order to get small fractures, which in the next step were embedded for further processing.

For embedding, the small fractures were placed in a silicon casting mold in a way, that the cross sections of the carrier material with two washcoats are located close to the tip of the mold. The mold was placed in a desiccator, which afterwards was evacuated. A two-component epoxy resin (Epoxy L & Härter L; R&G Faerverbundwerkstoffe
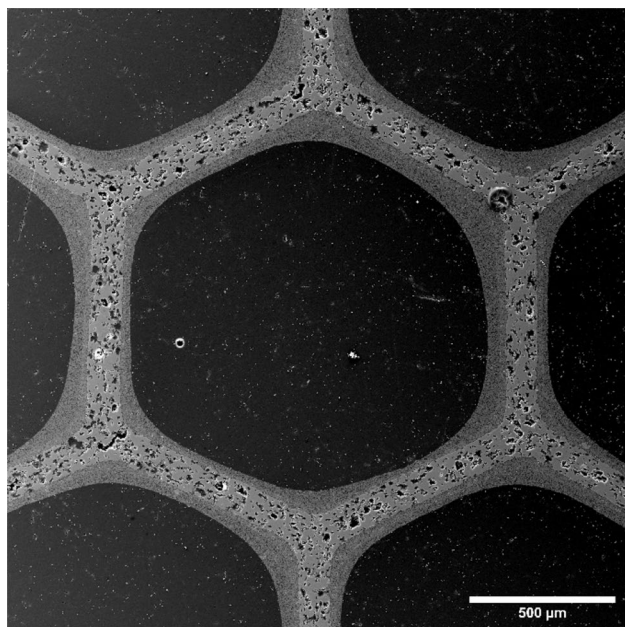
Fig. 1 SEM image of a channel cross section with a size of 2.1×2.1 mm showing the approximately circular channel and washcoat geometry

GmbH) was mixed (10:4) and the mold inside the desiccator was filled using a syringe so that the resin could invade the pores. After 8 h curing time, the mold was taken out of the desiccator and the samples were taken out of the mold.

To make the sample suitable for the Focused Ion Beam system (FIB), the backend of the samples was cut off using a razor blade. Further, it was necessary to uncover the regions of interest (ROI) of the samples, which were covered by thin layers of epoxy resin. This was achieved by grinding the tips using two different types of sandpaper (800 & 2000) and polishing using a diamond polishing paste (particle size 6 μm) on a glass slide.

The polished samples were glued to a 90° sample holder or clamped slotted sample holder. In both cases, silver paste was used to fix the samples and to provide a conductive connection between the sample and the holder.

In a final step, the samples were sputtered with a gold layer with a thickness of 20 nm (Sputter Coater 108 auto, Cressington) to provide a conductive surface.

2.1.2 FIB-SEM Tomography

The as prepared samples were transferred into the FIB system (Auriga 60, Carl Zeiss). The ROI was identified using the electron beam (3 kV acceleration voltage) and brought to the eucentric height. The ROI was placed perpendicular to the ion beam and in front of the ROI a trench was milled using the focused ion beam (beam current: 4 nA, 30 kV acceleration voltage). After milling of the trench, the ROI for the tomography was determined and a stack of slices was milled and corresponding images were taken. For that, the sample was cut using the ion beam (beam current 600 pA, 30 kV acceleration voltage, slice thickness: 70 nm) and imaged using the electron beam (3 kV acceleration voltage) with a pixel size of 20 nm.

2.1.3 Image Processing

In order to quantify the microstructure, the FIB-SEM tomography data undergoes various image processing steps. The images are aligned slice by slice using a plugin based on scale-invariant feature transformation [24] as well as coarsely cropped to the relevant region of interest (ROI) using the Fiji distribution of ImageJ. All further steps like fine crop, image segmentation as well as post processing are conducted using the current version of GeoDict® 2022. All FIB-SEM tomography data sets are treated identically, starting with slice thickness correction using nearest-neighbor interpolation in order to achieve cubic volumetric pixel (=voxel) of size 20×20x20 nm. Cubic voxels are used for the evaluation of the 3D structures. Because of the strong contrast between solid and pore phase, grey-value threshold
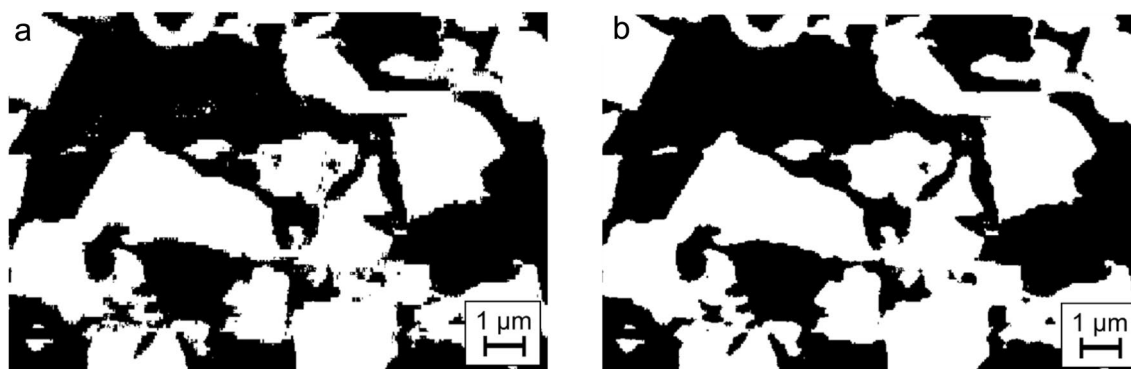
Fig. 2 Comparison of binary image before (**a**) and after (**b**) post-processing. Solid domains are colored in white and pore domains are colored in black. Small, unconnected artifacts are removed as well as a general denoising occurs during post-processing

Fig. 3 Schematic drawing of the workflow to prepare, image and analyze the wash coat structures. First, the sample was cut (**a**) and fractures were embedded (**b**). After mounting and sputter coating a trench was milled using a FIB-SEM-system (**c**). Afterwards slicing and imaging were performed, using a FIB-SEM-system (**d**). The resulting stack of images (**e**) were then processed using ImageJ and GeoDict.® 2022 leading to a filtered and aligned stack of tiff images which could be used for further analysis (**f**)
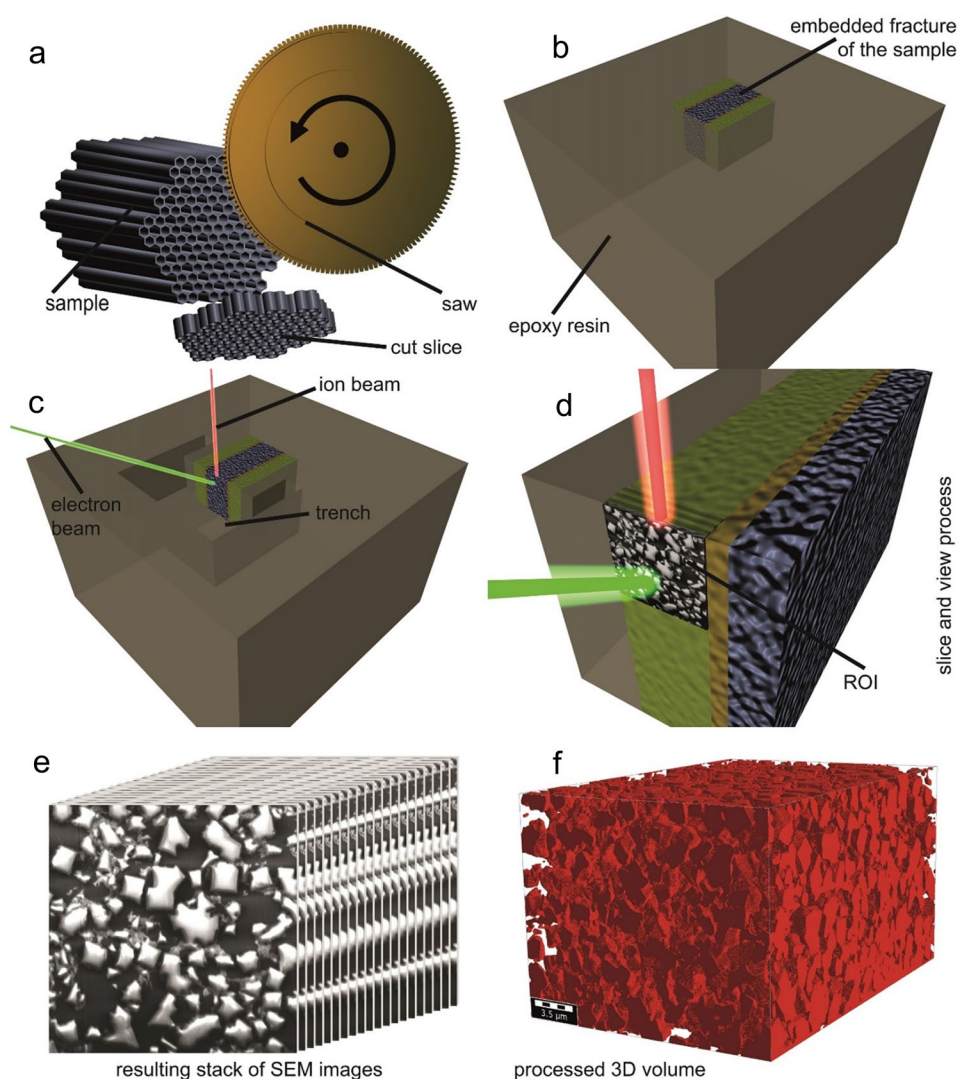
segmentation is sufficient for the image stack. After segmentation, the binarized microstructure, consisting of a solid as well as a pore phase, is post-processed by removing 3D unconnected solid phase artifacts as well as smoothing out noise at the edges of solid phase boundaries by morphological closing. The effects of the post-processing are shown in

Fig. 2. The entire process from sample preparation to the 3D voxel structure is shown in Fig. 3.

In a three-dimensional, binarized image, porosity is defined as the number of voxels attributed to pore space divided by the total number of voxels in the image. In addition to porosity, a transport limiting factor, known as the tortuosity factor is calculated using GeoDict® 2022 as well as the TauFactor application for MATLAB [25]. This factor considers the tortuousness of the pore space and its limiting influence on gas diffusion.

In the reconstruction process there are also floating particles to be considered. These can either be catalyst segments connected outside the domain covered by the FIB-SEM or artifacts from the tomography like residual debris of the slicing procedure and destroyed fragile structures during the pore filling. Figure S1 shows the floating particles of the reconstructed volume. Most of the bigger particles are located at the geometry borders and therefore are most likely connected to other zeolite particles outside of the boundary. The amount of smaller floating particles is insignificant and thus not further considered or removed.

2.2 Catalyst Performance Experiments

The performance of the model catalyst is measured by a CO oxidation light-off experiment. For this a cylindrical core with 1″ diameter and 1″ length is placed in a tubular flow-through quartz reactor. The catalyst is pretreated at 600 °C in 10% O_2 and 5% H_2O. After cooling down to the start temperature of 75 °C a gas mixture of 1050 ppm CO, 10% O_2 and 5% H_2O is fed into the reactor with a gas hourly space velocity of 300,000 h^{-1}. Then the light-off temperature ramp from 100 °C to 400 °C with 10 °C/min is performed and the gas phase composition monitored by a nondispersive infrared absorption analyzer (NGA 2000 MLT). This experiment is used to evaluate the diffusional resistance in the top layer of the dual layer catalyst. The bottom layer of the washcoat is relatively thin and we have shown in a previous simulation study that the internal diffusion resistance in this this layer is negligible [26]. Nevertheless, diffusion in the bottom layer is considered in the model with a porosity of 0.7 and a tortuosity of 10.

Ammonia oxidation tests are conducted on the same cylindrical 1″ × 1″ ASC catalyst to validate the results from the CO oxidation experiment. The core is placed in a different tubular flow-through quartz reactor and then pretreated at 500 °C in 10% O_2 and 5% H_2O. After cooling down to the start temperature of 150 °C a gas mixture of 300 ppm NH_3, 10% O_2 and 5% H_2O is fed into the reactor with a gas hourly space velocity of 300,000 h^{-1}. Then a light-off temperature ramp is performed from 150 °C to 500 °C using a ramp rate of 2 °C/min. The gas composition is monitored by a FTIR (Antaris™ IGS Gas Analyzer).

3 Models

3.1 Determination of Effective Diffusion Coefficients by Simulations in GeoDict® 2022 and TauFactor

In TauFactor [25] the conductivities at voxel faces are computed and the Laplace equation

$$\frac{\partial c}{\partial t} = D\left(\frac{\partial^2 c}{\partial x^2} + \frac{\partial^2 c}{\partial y^2} + \frac{\partial^2 c}{\partial z^2}\right) = 0 \tag{2}$$

is solved for the pore space, where c is the local concentration of the diffusing species with the diffusivity D and x, y, z the spatial directions. This is done directly on the voxel discretization obtained by the FIB-SEM measurements. Fixed concentration values (Dirichlet) are imposed as boundary conditions at the inlet and outlet face of the geometry thus creating a concentration gradient in one direction. Neumann boundary conditions ($\nabla c \cdot n = 0$) are used for all other faces. Effective diffusivity factors $D_{\text{eff}}/D_{\text{gas}}$ are computed along all three coordinates by repeating this procedure in all space directions, comparing the steady-state diffusive flow through a pore network to that through a fully dense control volume of the same size and diffusivity. The effective diffusivity factor is a dimensionless quantity $D_{\text{eff}}/D_{\text{gas}}$ that is only a property of the pore structure and thus independent of the diffusing species and surrounding fluid. GeoDict® 2022 essentially solves the same equations as TauFactor.

3.2 Reactor Model

A 1D + 1D model of a single channel is used to describe the catalyst. The channel as well as the washcoat layers are considered circular in shape which is close to reality due to the hexagonal shape of the model catalyst's channels. The channel is discretized in axial volume elements and the heat- and mass balances are solved for each volume element. These balances include convection, heat- and mass transfer between the gas and the washcoat, as well as the reactions in the washcoat. The simulator is used in [20, 27] and is described in more detail in [28]. The used gas phase diffusion coefficients are computed according to Fuller [28].

To simulate the CO oxidation, the reaction is only considered in the Pt-containing bottom layer and the SCR top layer is simulated as an inert diffusion barrier. A global rate equation is used to describe the CO oxidation:

$$r_{CO} = -k_{\text{CO}} \cdot x_{\text{g,CO}} \cdot x_{\text{g,O}_2} \cdot \frac{0.011}{G} \tag{3}$$

where r_{CO} is the consumption rate of CO, $x_{g,CO}$ and $x_{g,O2}$ are the gas mole fractions of CO and O_2, G is an inhibition term. The rate constants k_i are calculated according to:

$$k_i = k_{0,i} \cdot \exp\left(\frac{E_{A,i}}{R} \cdot \left(\frac{1}{T} - \frac{1}{T_{\text{ref}}}\right)\right) \tag{4}$$

with the pre-exponential factors $k_{0,i}$ and the activation energies $E_{A,i}$ which are listed in Table 1. The reference temperature T_{ref} is 450 K. The inhibition term G is:

$$G = T \cdot \left(1 + k_1 \cdot x_{g,CO}\right)^2 \cdot \left(1 + k_2 \cdot x_{g,CO}^2\right) \tag{5}$$

The kinetic parameters were fitted to the CO oxidation experiment of the dual layer ASC described in the catalyst performance testing section.

For the simulations of the ammonia oxidation experiment the dual layer catalyst model described in [20] is applied. The SCR layer is described by a global model for the SCR reactions on Cu-chabazite developed by Bendrich et al. in [27] based on the rate equations discussed in [30]. The Pt-layer is described by the kinetic model provided in [31]. Both mechanisms were pre-calibrated to experimental data of single layer platinum- and SCR catalysts respectively. The kinetic parameters were then fine-tuned to the data measured on the dual layer catalyst.
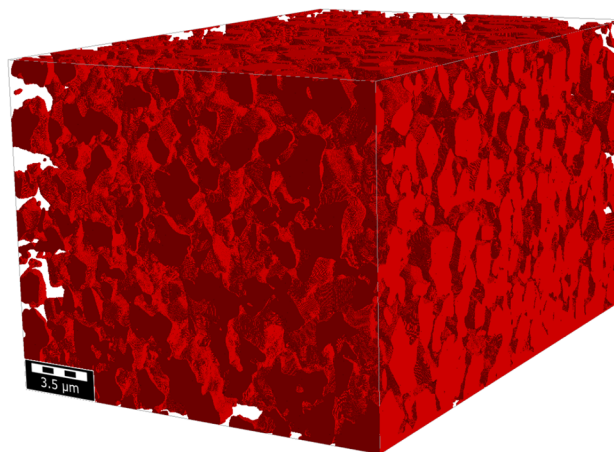
4 Results and Discussion

4.1 Determination of Effective Diffusion Coefficients From the 3D Pore Structure Reconstructed From FIB-SEM Data

Figure 4 shows one exemplary reconstructed 3D voxel structure obtained by FIB-SEM slice&view tomography. For the tomography a slice from the monolithic catalyst sample was cut off—specifically a part of the substrate wall with exposed dual layer washcoat. The region of interest was the top washcoat layer. After processing and aligning the resulting image stack, a rectangular block of the macropore space is obtained with a cubic voxel size of $20 \times 20 \times 20$ nm^3 and a total volume of $20.28 \times 16.64 \times 29.28$ μm^3 in this exemplary case.

**Fig. 4** Physical reconstruction of the pore space of a monolithic ASC catalyst sample by FIB-SEM tomography. The solid phase is shown in red

The porosity of the volume is calculated by dividing the number of void voxels by the total amount of voxels. The resulting porosity of the exemplary sample is 51.3%. Diffusion simulations are used to determine the tortuosity factor τ of the domain. The tortuosity factor is calculated along the z-axis defined as the radial direction perpendicular to the flow in the monolith. The resulting concentration profile in the exemplary structure calculated from GeoDict® 2022 is shown in Fig. 5. Tortuosity factors for the 6 different washcoat sections analyzed by FIB-SEM are compared in Table 2. Both simulation tools—GeoDict® 2022 and the open-source MATLAB application TauFactor—give similar results, which is expected due to their similarity. The 6 tomography reconstructions of the upper layer are done at different positions of the channel geometry (corners and edges) as well as distances to the open channel and the AOC layer. The height/width of the tomographic reconstructions is on average ∼20 μm which corresponds to roughly one
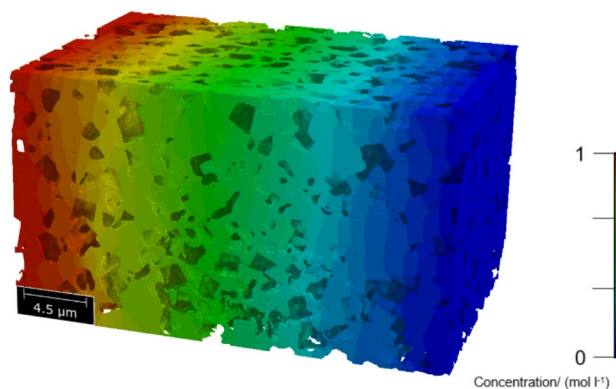
Fig. 5 Solved concentration profile along the z-axis of the exemplary structure taken from GeoDict.® 2022

Table 1 Kinetic parameters of the CO Oxidation

Parameter	Value	Parameter	Value/J/mol
$k_{0,CO}$	$1.08 \cdot 10^8$ K mol m^{-3} s^{-1}	$E_{A,CO}$	179,200
$k_{0,1}$	$8.84 \cdot 10^3$	$E_{A,1}$	− 3783
$k_{0,2}$	$1.94 \cdot 10^{11}$	$E_{A,2}$	− 105,808

Table 2 Determined porosity and tortuosity factors for 6 tomography reconstructions in GeoDict® and TauFactor as well as the resulting diffusivity factors

	ε/%	τ GeoDict	τ TauFactor	D_{eff}/D_{gas} GeoDict	D_{eff}/D_{gas} TauFactor	Volume/10^3 µm^3
Cut 1	56.2	1.62	1.62	0.35	0.35	8.94
Cut 2	52.5	1.75	1.72	0.30	0.31	11.17
Cut 3	49.2	1.94	1.88	0.25	0.26	6.53
Cut 4	51.3	1.68	1.65	0.31	0.31	9.88
Cut 5	50.0	1.87	1.83	0.27	0.27	9.26
Cut 6	56.9	1.53	1.49	0.37	0.38	17.22
Average	0.53	1.73	1.70	0.31	0.31	10.50
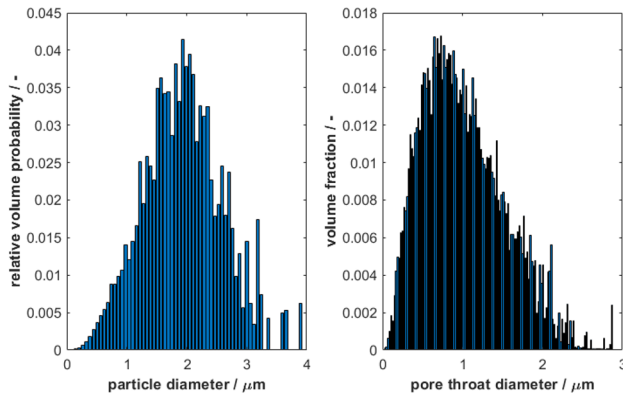
Fig. 6 Relative particle size (left) and pore size distributions (right) taken from GeoDict.® 2022 for Cut 4

third of the average washcoat thickness. Therefore, the sections should be sufficiently large to provide a statistical representation mitigating local effects.

Additionally, the pore and particle size distributions of the structures can be calculated from the 3D structures in GeoDict® 2022 and are shown in Fig. 6 exemplary for Cut 4. The cumulative pore size distribution yields d10 = 0.40 µm, d50 = 0.95 µm and d90 = 1.77 µm. The mean intermediate diameter of the particle size distribution is 1.91 µm.

One possible error source in the analysis of the FIB-SEM data is the choice of the threshold for the segmentation process. To investigate the effect of this choice on the obtained diffusivities, the segmentation was repeated using extreme threshold values. A comparison between the original SEM picture and the segmentation obtained using different thresholds is shown in Fig. 7.

Using an extreme value of the threshold reduces the porosity of the structure significantly from 51.3% to 41.5% and increases the tortuosity from 1.65 to 1.96. This causes the relative effective diffusivity D_{eff}/D_{gas} to change from 0.31 to 0.21. Even with this distinctly lower threshold the calculated diffusivity is still twice the diffusivity from the simulated light-off experiments.

4.2 Determination of Effective Diffusion Coefficients from CO Oxidation Measurements on the Dual Layer Catalyst

In addition to the FIB-SEM measurements, to determine the effective diffusion coefficient of the upper layer, performance measurements on the dual layer catalyst were performed under conditions where the overall conversion is mainly controlled by the diffusion in the top layer. A first set of experiments applied CO oxidation that only occurs in
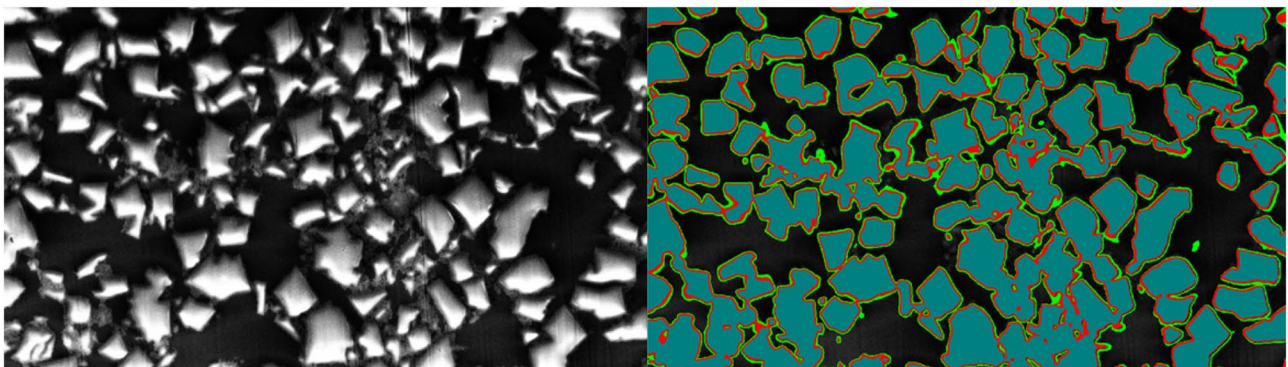
Fig. 7 Left side: Greyscale SEM picture of FIB-SEM tomography; right side: segmentation with higher threshold (cyan), chosen threshold (red), lower threshold (green)
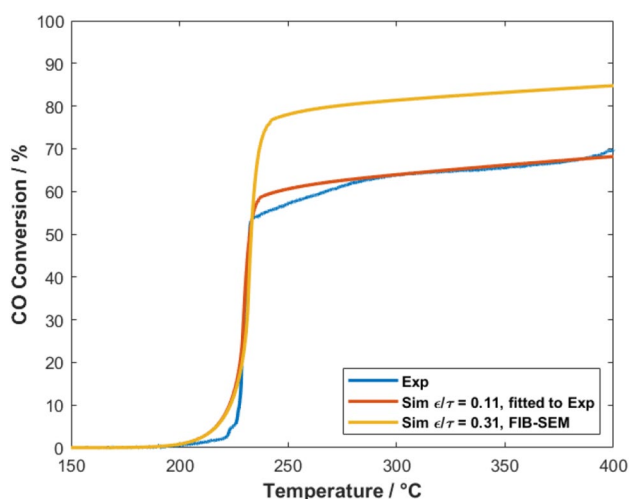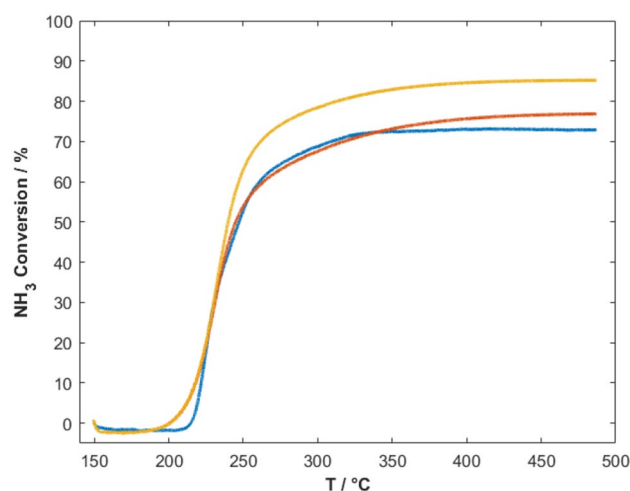
Fig. 8 Experimental data (blue) as well as simulation with FIB-SEM based (yellow) and fitted (red) diffusivity factor of the CO conversion in the CO oxidation experiment

Fig. 9 Experimental data (blue) as well as simulation with FIB-SEM based (yellow) and fitted to the CO experiment (red) diffusivity factor in the ammonia light-off experiment

the lower layer so that the upper layer acts as a pure diffusion barrier. It has been verified in separate CO oxidation experiments with just the SCR layer, that the Cu-SCR layer is inactive for CO oxidation. A typical experimental result of the dual layer CO oxidation measurement is shown in Fig. 8. After a light-off at ~232 °C, the CO conversion reaches a plateau and the conversion in this plateau is to a large extend determined by diffusion in the top layer. A diffusivity factor D_{eff}/D_{gas} of 0.11 is determined by fitting the kinetic model to reproduce the plateau. Figure 8 shows the simulated CO light-off curve obtained with the adjusted diffusivity factor of 0.11, as well as a simulation performed with the average diffusivity factor of 0.31 obtained from the FIB-SEM measurement. Obviously, the diffusivity factor obtained by FIB-SEM is significantly too high to reproduce the experimental result.

4.3 Validation by Simulating NH3 Oxidation Measurements on the Dual Layer Catalyst

Besides the CO oxidation experiments, also NH$_3$ oxidation experiments have been performed on the dual layer catalyst. A typical result is shown in Fig. 9. The interpretation of these experiments is less straightforward than that of the CO oxidation experiments, since now also the upper layer contributes to the overall conversion by reacting NO formed in the lower with counter-diffusing NH$_3$. However, previous simulation studies [20, 22] have shown that at high temperatures, the NH$_3$ oxidation is nearly entirely determined by the effective diffusivity in the upper SCR layer. Simulating the experiment using the diffusivity factor D_{eff}/D_{gas} of 0.11 obtained from the CO oxidation experiment well reproduces the plateau in the NH$_3$ conversion observed in

the experiment. In turn, simulating the experiment using the diffusivity factor obtained by the FIB-SEM measurements significantly overestimates the conversion in the plateau, indicating that the results obtained for the NH$_3$ oxidation are consistent with the results for the CO oxidation.

4.4 Comparison of Effective Diffusion Coefficients from FIB-SEM and CO Oxidation Experiments

In Table 3 we compare the effective diffusivity obtained in this work with the diffusivities of zeolite layers reported by other authors. These diffusivities reported in literature were obtained either by lab reactor performance measurements of the SCR reaction in single layer catalysts with different washcoat thicknesses ([16] Cu-zeolite; [27] Cu-chabazite), or by performance measurements on dual layer catalysts ([23] NH$_3$ oxidation on ZSM-5 and Pt/Al$_2$O$_3$ dual layer; [20] NH$_3$ oxidation on Fe-zeolite and Pt/Al$_2$O$_3$). Apparently, the diffusivities obtained in this paper are in line with the values

Table 3 Comparison of the effective diffusivity factors D_{eff}/D_{gas} and the tortuosity factors τ obtained in this work for with values obtained in the literature for different zeolite washcoat layers. The diffusivity for Nova et al. was calculated assuming the NO gas phase diffusion coefficient at 200 °C computed according to [29]

	D_{eff}/D_{gas}	τ	Zeolite
This work, FIB-SEM	**0.31**	**1.73**	Cu-chabazite
This work, CO oxidation exp	**0.11**	**4.80**	Cu-chabazite
Nova et al. [16]	0.06	5.00	Cu-zeolite
Scheuer et al. [20]	0.07	10.00	Fe-zeolite
Dhillon et al. [22]	0.03	9.60	ZSM-5
Bendrich et al. [27]	0.09	5.05	Cu-chabazite

reported in the literature, with the diffusivities in the literature even being lower than our values. On the other hand, the diffusivities obtained based on our FIB-SEM analysis are a factor of three higher than our values obtained from the CO oxidation measurements. This inconsistency becomes even more obvious if one compares the tortuosity factors. With a tortuosity factor of 1.73, the FIB-SEM data predict a diffusivity not too far from the maximum possible value of $\tau = 1$, indicating only minor obstruction of the diffusion paths through the pore network. The tortuosity factors obtained from performance measurements are a factor of more than 3 larger, indicating significant obstruction of the diffusion path by the pore geometry.

The observed inconsistency between the diffusivities obtained by the FIB-SEM analysis and the diffusivities obtained from catalyst performance measurements is clearly beyond the expected statistical uncertainty of the two methods. Therefore, potential systematic error sources of both methods need to be investigated. In the FIB-SEM analysis, the most severe systematic error source are typically segmentation errors, which we tried to estimate and which do not explain the differences between both methods. A potential source of uncertainty in the determination of the effective diffusion coefficients from the performance measurements are chemical interactions of the two layers in the dual layer catalyst, so that the activity of the individual layers might be altered in the dual layer system. But this would not explain the low diffusivities observed in the single layer studies of [16], as well as the fact that the low diffusivity has been consistently observed for different dual layer systems (Cu-exchanged zeolite in this paper vs. Na-exchanged ZSM-5 in [23]). Furthermore, relatively low effective diffusivity factors such as those reported in Table 3 are generally applied in models of SCR- and dual layer ammonia oxidation catalysts and these seem to yield consistent results. Our FIB-SEM results provide some motivation to question the apparent consensus in the modelling community and to investigate whether equally consistent descriptions could be obtained using higher effective diffusion coefficients. To exclude chemical interaction between the washcoat layers as a potential error source, we are currently repeating the performance measurements on a dual layer catalyst using a Cu-free zeolite layer.

Also, the experimental FIB-SEM procedures as well as the data analysis leading to the effective diffusion coefficients need to be further critically evaluated. The microstructure obtained by FIB-SEM should be compared with the structure obtained by other methods such as nano-tomography or ptychography, as well as with 3D structures reconstructed from 2D SEM data.

The results of this work highlight the need for further work towards a consistent μ-scale description of pore diffusion in monolith catalysts. Once a consistent scale-bridging description has been achieved, pore scale models in combination with FIB-SEM- and other 3D imaging techniques will be a very useful technique, not only to provide independent estimates of the effective diffusivity as input for macroscopic reactor simulations, but also for a systematic optimization of catalyst microstructure, leading to an improved catalyst effectiveness.

5 Conclusion

We used FIB-SEM tomography to determine the 3D pore structure of the upper Cu-chabazite layer in a dual layer ammonia oxidation catalyst. On the reconstructed pore structure diffusion simulations were carried out to determine its effective diffusivity. With a tortuosity factor of 1.73 and a diffusivity factor D_{eff}/D_{gas} of 0.31, the obtained diffusivity is significantly higher than diffusivities of zeolite washcoats reported in the literature and the diffusivity factors used by the modelling community. CO oxidation measurements performed on the dual layer catalyst yielded a diffusivity in line with the literature values and a factor of three lower than the value obtained for the same catalyst by FIB-SEM. NH_3 oxidation experiments performed on the dual layer catalyst could be well modelled using the diffusivity obtained by the CO oxidation experiments while no satisfactory description of the experimental NH_3 conversion could be obtained if the diffusivity determined from the FIB-SEM analysis was used in the simulations.

The origin of the inconsistency between the diffusivities obtained from the FIB-SEM analysis and the diffusivities observed in catalyst performance measurements remains not understood for the moment. This will require further work in the future. Understanding the observed inconsistency will be a crucial step towards simulation models that yield a truthful description of pore-scale transport. Such models will allow a rational optimization of catalyst structure on the micro-scale which will ultimately lead to increased catalyst effectiveness.

Declarations

References

1. Dhillon PS, Harold MP, Wang D, Kumar A, Joshi S (2019) Catal Today 320:20–29. https://doi.org/10.1016/j.cattod.2017.12.023
2. Kato S, Yamaguchi S, Uyama T, Yamada H, Tagawa T, Nagai Y, Tanabe T (2017) Chem Eng J 324:370–379. https://doi.org/10.1002/cctc.201800230
3. Becher J, Sheppard TL (2019) Fam y; Baier S, Wang W, Wang D, Kulkarni S, Keller TF, Lyubomirskiy M, Brueckner D, Kahnt M, Schropp A, Schroer CG, Grunwaldt, JD. J Phys Chem C 123:25197–25208. https://doi.org/10.1021/acs.jpcc.9b06541
4. Stoeckel D, Kübel C, Hormann K, Höltzel A, Smarsly BM, Tallarek U (2014) Langmuir 30:9022–9027. https://doi.org/10.1021/la502381m
5. Kroll M, Hlushkou D, Schlabach S, Höltzel A, Roling B, Tallarek U (2018) J Electrochem Soc 165:A3156. https://doi.org/10.1149/2.0711813jes
6. Hlushkou D, Reising AE, Kaiser N, Spannenberger S, Schlabach S, Kato Y, Roling B, Tallarek U (2018) J Power Sources 396:363–370. https://doi.org/10.1016/j.jpowsour.2018.06.041
7. Kroll M, Karstens SL, Cronau M, Höltzel A, Schlabach S, Nobel N, Redenbach C, Roling B, Tallarek U (2021) Batteries Supercaps 4:1363–1373. https://doi.org/10.1002/batt.202100057
8. Reising AE, Schlabach S, Baranau V, Stoeckel D, Tallarek U (2017) J Chromatogr A 1513:172–182. https://doi.org/10.1016/j.chroma.2017.07.049
9. Greiner R, Prill T, Iliev O, van Setten BAAL, Votsmeier M (2019) Chem Eng J 378:121919. https://doi.org/10.1016/j.cej.2019.121919
10. Belot I, Vidal D, Greiner R, Votsmeier M, Hayes RE, Bertrand F (2021) Chem Eng J 406:127040. https://doi.org/10.1016/j.cej.2020.127040
11. Plachá M, Kočí P, Isoz M, Svoboda M, Price E, Thompsett D, Kallis K, Tsolakis A (2020) Chem Eng Sci 226:115854. https://doi.org/10.1016/j.ces.2020.115854
12. Kočí P, Novák V, Štěpánek F, Marek M (2010) M Kubíček. Chem Eng Sci 65:412–419. https://doi.org/10.1016/j.ces.2009.06.068
13. Novák V, Kočí P, Marek M, Štěpánek F, Blanco-García P, Jones G (2012) Catal Today 188:62–69. https://doi.org/10.1016/j.cattod.2012.03.049
14. Novák V, Dudák M, Kočí P, Marek M (2015) Curr Opin Chem Eng 9:16–26. https://doi.org/10.1016/j.coche.2015.07.002
15. Karakaya C, Weddle PJ, Blasi JM, Dircks DR, Kee RJ (2016) Chem Eng Sci 145:299–307. https://doi.org/10.1016/j.ces.2016.02.004
16. Nova I, Bounechada D, Maestri R, Tronconi E, Heibel AK, Collins TA, Boger T (2011) Ind Eng Chem Res 50:299–309. https://doi.org/10.1021/ie1015409
17. Metkar PS, Salazar N, Muncrief R, Balakotaiah V, Harold MP (2011) Appl Catal B 104:110–126. https://doi.org/10.1016/j.apcatb.2011.02.022
18. Yu S, Zhang J (2021) Processes 9:1966. https://doi.org/10.3390/pr9111966
19. Colombo M, Nova I, Tronconi E (2012) Chemi Eng Sci 75:75–83. https://doi.org/10.1016/j.ces.2012.02.044
20. Scheuer A, Hauptmann W, Drochner A, Gieshoff J, Vogel H, Votsmeier M (2012) Appl Catal B 111–112:445–455. https://doi.org/10.1016/j.apcatb.2011.10.032
21. Shrestha S, Harold MP, Kamasumudram K, Kumar A, Olsson L, Leistner K (2016) Catal Today 267:130–144. https://doi.org/10.1016/j.cattod.2015.11.035
22. Dhillon PS, Harold MP, Wang D, Kumar A, Joshi SY (2019) React Chem Eng 4:1103–1115. https://doi.org/10.1039/C8RE00325D
23. Shrestha S, Harold MP, Kamasamudram K (2015) Chem Eng J 278:24–35. https://doi.org/10.1016/j.cej.2015.01.015
24. Lowe DG (2004) Int J Comput Vis 60:91–110. https://doi.org/10.1023/B:VISI.0000029664.99615.94
25. Cooper SJ, Bertei A, Shearing PR, Kilner JA, Brandon NP (2016) SoftwareX 5:203–210. https://doi.org/10.1016/j.softx.2016.09.002
26. Votsmeier M, Scheuer A, Drochner A, Vogel H, Gieshoff J (2010) Catal Today 151:271–277. https://doi.org/10.1016/j.cattod.2010.01.018
27. Bendrich M, Scheuer A, Votsmeier M (2020) Catal Today 360:252–262. https://doi.org/10.1016/j.cattod.2020.03.015
28. Hauptmann W, Votsmeier M, Vogel H, Vlachos DG (2011) Appl Catal A-Gen 397:174–182. https://doi.org/10.1016/j.apcata.2011.02.031
29. Fuller EN, Schettler PD, Giddings JC (1966) Ind Eng Chem 58:18–27. https://doi.org/10.1021/ie50677a007
30. Schuler A, Votsmeier M, Kiwic P, Gieshoff J, Hauptmann W, Drochner A, Vogel H (2009) Chem Eng J 154:333–340. https://doi.org/10.1016/j.cej.2009.02.037
31. Scheuer A, Votsmeier M, Schuler A, Gieshoff J, Drochner A, Vogel H (2009) Top Catal 52:1847–1851. https://doi.org/10.1007/s11244-009-9351-9